International Journal of Mechanical Sciences 204 (2021) 106577

Contents lists available at ScienceDirect

International Journal of Mechanical Sciences

journal homepage: www.elsevier.com/locate/ijmecsci

Mesh-free micromechanical modeling of inverse opal structures

Maksym Dosta [a,*], Katrin Bistreck [a], Vasyl Skorych [a], Gerold A. Schneider [b]

[a] Hamburg University of Technology, Institute of Solids Process Engineering and Particle Technology
[b] Hamburg University of Technology, Institute of Advanced Ceramics

ARTICLE INFO

Keywords:
Metamaterials
Bonded particle method
Inverse opal
Fracture behavior
Discrete element method

ABSTRACT

The application of mesh-free discrete element method (DEM) for modeling of macroporous inverse opals is proposed. The developed and implemented DEM-based strategy is applied to analyze stiffness and strength of inverse opals made of pure silica and inverse opals coated with titania layers of various thicknesses. Also, the influence of the porosity of the initial packing on the properties of the material is investigated. Simulation results have shown that due to the heterogeneous macroscopic structure and unequal material distribution in nodes, struts or near interstitial pores, strong inhomogeneities of the stress distribution arise. Spots of localized stresses located near the interpore openings are the sources of initial defects and small interpore cracks. Reducing the overall porosity or an additional coating of the structure with a titania layer allows to partially homogenize and improve its mechanical properties.

It was shown that the obtained simulation results are in very good agreement with previous studies. Despite large computational effort, the performed analysis confirms the high efficiency of the proposed DEM-based approach and demonstrates its great potential for use in problems of a similar class: for modelling of complex-structured multicomponent materials.

1. Introduction

Inverse opals are a class of metamaterials with highly-ordered macropores. They are widely used in different areas and have various applications, such as optical [36], chemical [63] or thermal [61]. In most of them, the mechanical properties of materials, as well as the ratio of stiffness or strength to density, play an important role. Therefore, in recent years, a large number of studies have been focused on the analysis of the mechanical properties of various types of lightweight metamaterials [5,30,43] and especially inverse opals [54,57,58]. The inverse opals can be fabricated as closed-cell or open-cell structures. Although the closed-cell structures outperform open-cells [8], in most cases open-cell structures are used. To improve their mechanical properties an additional coating with stiffer and stronger material can be effectively employed. Previous investigations [56], have shown that due to nearly isotropic material response, the resulted material can possess exceptional properties which can outperform strut-based and honeycomb structures [57] rivaled only by anisotropic honeycomb structures [6].

From a numerical point of view, due to its robustness and versatility, the finite element method (FEM) is one of the most widely used approaches for studying the mechanics of such porous and cellular materials. With respect to sample size there can be distinguished three main strategies to represent material microstructure [13]: multi-cell models of finite samples, unit-cell models where a single or limited number of periodic base-cells are modeled, and embedded-cell models as combination of both types. In the case of multi-cell models, a relatively large sample is modeled to minimize size-effects and, as consequence, this can lead to high computational costs [26,37,47,71]. In order to reduce computational effort for low density open-cells foams or lattice-type structures, simplified geometrical models [12] can be applied. Alternatively, the application of unit-cell models, where the material is modeled with the representative volume element (RVE), allows to perform FEM calculations with high geometric detail and relatively low computational effort. Such unit-cells can be generated for periodic homogeneous structures as well as for heterogeneous materials [4].

Overall, one of the central questions addressed with the numerical studies is the investigation of structure-property relationships, like influence of the solid fraction on Young's modulus or plateau stress [22,27]. In recent years a lot of research was done focused on metallic foams, where various aspects such as structural irregularities [42], cell geometries [38], pore connectivity [41], plastic properties of cell wall material [34], shape anisotropy [28], etc. were investigated. Furthermore, FEM has also been applied for inverse opal structures. Cho et al. [10] used it to gain insights into the mechanical response of SU-8 inverse opals. Pikul et al. [48] described with FEM the stresses occurring in the nickel-based cellular material. Do Rosario et al. [57] and Cho et al. [9] utilized FEM to simulate the mechanical response of bi-layered inverse opals.

* Corresponding author at: Denickestrasse 15, 21073 Hamburg, Germany.
E-mail address: dosta@tuhh.de (M. Dosta).

https://doi.org/10.1016/j.ijmecsci.2021.106577
Received 20 October 2020; Received in revised form 25 May 2021; Accepted 1 June 2021
Available online 5 June 2021

In the studies mentioned above, it was shown that the finite element method can be effectively applied to such structures while providing reliable results.

Despite all the advantages, the use of FEM is often associated with significant challenges when modeling large deformations or fractures. There exist alternative approaches that allow to consider fracture, such as extended finite element method, cohesive zone model [70], peridynamics [3] or some hybrid strategies [21]. One of the very promising modeling approaches that can be effectively used to investigate the mechanical properties of complex-structured and heterogeneous materials is the mesh-free bonded-particle model (BPM).

The BPM is an extension of a soft-sphere discrete element method (DEM), where each pair of particles can be connected by a solid bond [50], which makes it possible to describe objects of complex shapes. The overall behavior of the material is described by constitutive models of particles interaction and by single solid bond models. The possibility to remove individual solid bonds during the simulation allows one to explicitly simulate fracture of the material without any additional remeshing. In recent years, this approach has been applied to various materials, such as silica glass, porous ceramics, concrete, aerogels, wood chips, etc. [2,15,32,33,35,39,45,51,55,69]. The main advantages of the BPM approach are:

- high flexibility during generation of a structural model: each particle or bond can have its unique material or geometrical properties;
- possibility to simulate material fracture: the fracture in BPM is modeled explicitly, starting with the initial crack formation, their propagation and ending with the overall fracture;
- possibility to use any type of functional model: there is no limitations on the type of functional relationships to describe the behavior of each single discrete object.

Among the main drawbacks of the BPM approach, one can emphasize high computational effort caused by a large number of modeled objects and the need to adjust model parameters. While in the case of FEM relatively small RVE are used, larger domains are needed for BPM calculations. Furthermore, due to the discrete nature and non-uniform positioning of primary particles, there are still no effective strategies to run BPM simulations with periodic conditions. To compensate for the high computational effort of mesh-free BPM method, parallelization for graphics processing units can be applied [16].

In this contribution, a BPM-based simulation strategy is proposed for modeling inverse opals. Using this strategy, samples consisting of pure SiO_2 were simulated, and the influence of an additional coating layer of TiO_2 and the behavior of the material with different porosities for low strains were investigated. The experimental results of do Rosario et al. [57] were used as reference data. There, the reference structure was built by vertical co-assembly based on the procedure of Hatton et al. [24]. The resulting silica structures exhibited FCC-disposed (face-centered cubic) spherical macro pores with a diameter of 756 ± 20 nm. Some samples were coated using atomic layer deposition (ALD) with an amorphous layer of titanium dioxide with a thickness of 10, 20 or 34 nm. In all cases, the pores were interconnected by holes. The prepared samples were cut into pillars with a height of 3 to 4.7 μm and an area of 66.9 to 135.1 μm^2 (Fig. 1). Using nanoindentation, both stiffness and strength of these pillars were determined. Further information about this study of inverse opals can be found in do Rosario et al. [57].

2. Modelling approach

2.1. Structural model

The generation of all studied structures was carried out identically as follows. Firstly, initial random packings consisting of spherical particles with a diameter of 15 nm were produced. The particles were generated with a force-based algorithm [16] in a cuboid of the required size to produce bulk with initial porosity of 0.38. The axial periodic boundary conditions (PBC) were applied in two directions – X and Y. The selected particle size of 15 nm does not exactly reproduce the microstructure of the material, however such size was selected as a compromise between the complexity of the simulation and its resolution: smaller diameters lead to an increase in the number of discrete objects, which causes high demands on computing resources and long simulation times, while an increase in the particle size results in a degradation of the model's accuracy and a decrease in the detail of the simulation results. It will be shown that the selected particle size is a fine enough to model the homogenous material.

To calculate the final positions of particles, an iterative force-biased algorithm implemented in the open-source MUSEN simulation framework was applied. Its detailed description can be found in Dosta et al. [17]. Compared to the previous version used in the publication, the package generation algorithm was improved by introducing GPU parallelization, which allowed to generate large packages in a reasonable time (up to 14.1 million primary particles in this study).

After the generation of cuboid packing, some fraction of primary particles were cut out of the packages to form pores. Structures with two types of pore arrangement were generated: ordered according to the face-centered cubic (FCC) lattice and randomly placed. For the first case, the coordinates of the spherical pores to be cut were calculated directly. In the second case, they were generated in MUSEN using the same strategy and the force-biased algorithm as for the generation of primary particles in initial packings. A similar DEM-based approach was used in previous studies to generate a realistic microstructure of the material [16,47]. For all simulations, the pore diameter was set to 762 nm. For samples without coating, all particles for which the condition

$$L = \left|\bar{X}_{pore} - \bar{X}_{part}\right| \leq R_{pore} + R_{part} \tag{1}$$

was satisfied, were removed from the initial packages. Here, $\bar{X}_{pore}$ and $\bar{X}_{part}$ are coordinates of a pore and a particle, respectively, R_{pore} and R_{part} are their radii, and L is a distance between them. In the case of coated samples, it was necessary to perform several additional steps to generate a titania layer. Firstly, depending on the coating thickness L_{coat}, all particles from initial package that satisfy condition

$$R_{pore} + R_{part} - L_{coat} \leq L \leq R_{pore} + R_{part} \tag{2}$$

were marked as potentially belonging to the titania layer. The second step was necessary to properly consider effect, that due to the ALD-coating, the pores remain connected by interpore openings. To ensure this, particles lying on the boundary of each pore were detected. Then, all the obtained titanium dioxide particles were analyzed once again to find those that lie farther from the surface of any pore then $L_{coat} + R_{part}$. Removing those ensured that the interpore openings remained free. Finally, all the particles that satisfy condition (1) but do not satisfy (2) were considered as pores and cut out of the sample.

The two bottom layers of particles were defined as a fixed substrate. For this purpose, they were assigned an artificially high density, which prevented the movement of these particles during the simulation.

Finally, the remaining particles were connected by solid bonds. They were generated between all pairs of particles located at a distance of less than 26.25 nm, which corresponds to a maximum length of 1.75 times the particle diameter. The axial periodic boundary conditions were taken into account during the generation of bonds and they were also created across the boundaries. This made it possible to obtain good connectivity in the structure and led to an average coordination number of about 10.5. For the uncoated structures, all bonds were made of silica. For the coated samples, two types of bonds were generated: silica bonds between silica particles and between silica and a fixed layer and titania bonds between titania particles, titania and silica, as well as between titania and a fixed layer. This means that the interfacial zone between titania and silica was not explicitly resolved and was considered to have the same properties as titania.

Using the proposed strategy, the average number of primary particles and solid bonds that are needed to represent 1 μm^3 of FCC-ordered

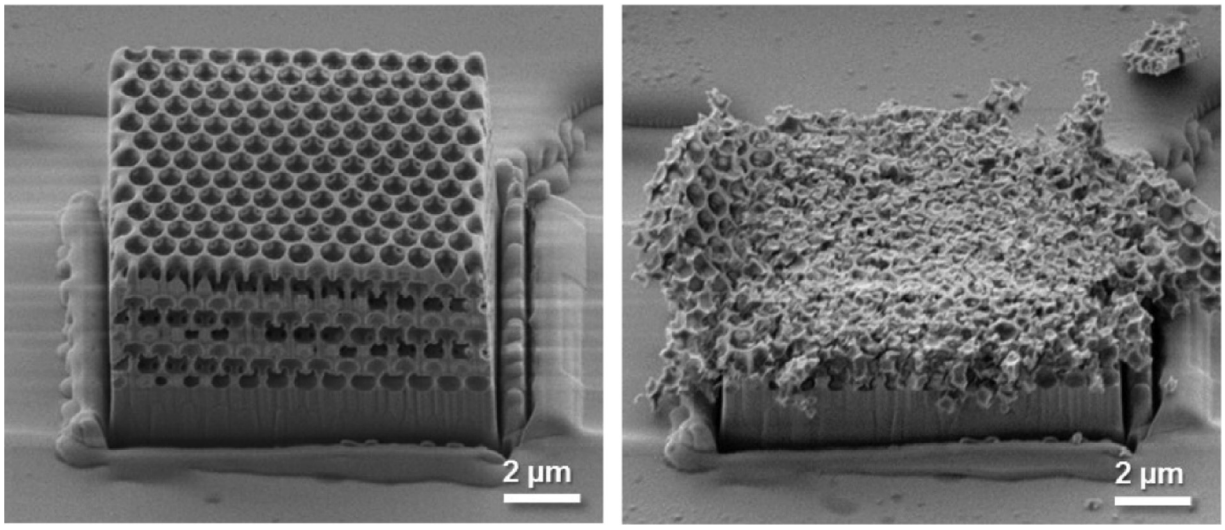

Fig. 1. Fabricated micropillars for uncoated silica inverse opals before and after fracture [57].

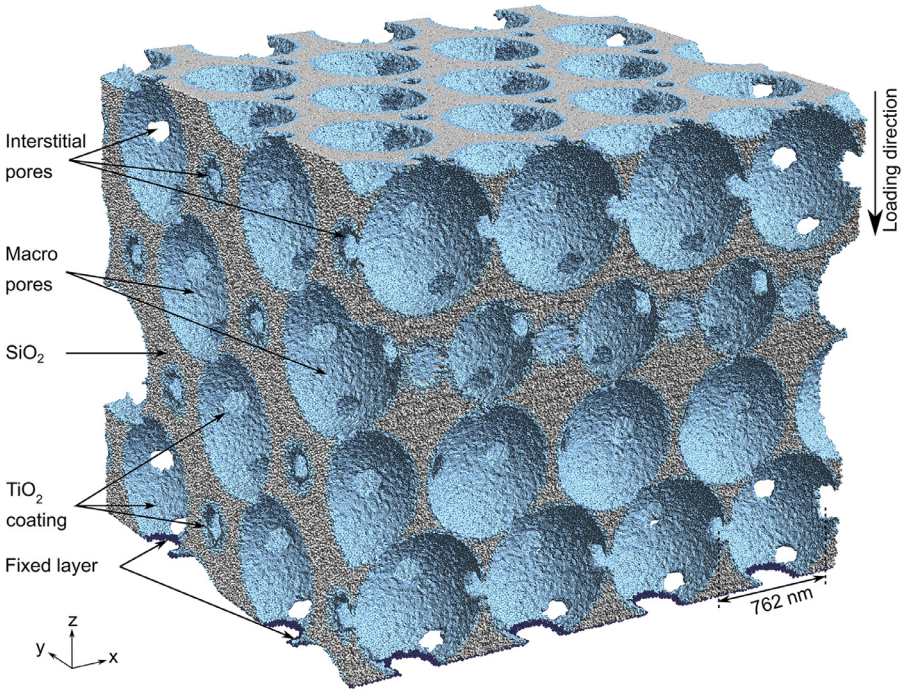

Fig. 2. Representation of the material microstructure using a bonded-particle model. The inverse opal silica is coated with a 20 nm thick layer of TiO2.

inverse opals without coating is 80 000 and 843 000 respectively. Fig. 2 shows the final BPM structure of a SiO_2 sample coated with a TiO_2 layer with thickness of 20 nm. The depicted structure consists of about 2.5 million particles and 27.2 million bonds.

Finally, to simulate the uniaxial compression test, the structural model was supplemented with a diamond plate above the structure moving in the vertical direction and compressing the inverse opal.

2.2. Functional model and implementation aspects

Forces and moments acting in the simulated material are described by three different types of contact models (Fig. 3): particle-particle, particle-wall and solid bond. Particle-particle and particle-wall interactions are modeled by the non-linear viscoelastic Hertz-Mindlin model [44,66]. The model is applied only for pairs of particles between which there is no solid bond, as well as for all contacts between particles and walls. The effect of solid bonds is described based on the ideally elastic model [14,50].

The total force ($\vec{F}_{tot,i}$) and the moment ($\vec{M}_{tot,i}$) that act on each primary particle are calculated as:

$$\vec{F}_{tot,i} = \sum_{j=1}^{N_{pp,i}} \vec{F}_{pp,i:j} + \sum_{j=1}^{N_{pw,i}} \vec{F}_{pw,i:j} + \sum_{j=1}^{N_{sb,i}} \vec{F}_{b,i:j} + \vec{F}_g \tag{3}$$

$$\vec{M}_{tot,i} = \sum_{j=1}^{N_{pp,i}} \vec{M}_{pp,i:j} + \sum_{j=1}^{N_{pw,i}} \vec{M}_{pw,i:j} + \sum_{j=1}^{N_{b,i}} \vec{M}_{b,i:j} \tag{4}$$

where $N_{pp,i}$ and $N_{pw,i}$ are the number of active particle-particle and particle-wall contacts, respectively; $N_{b,i}$ is the number of solid bonds connected to the particle; $\vec{F}_{i:j}$ is the force acting between objects i and j; $\vec{F}_g$ is the gravity force.

During the computations, the forces are decomposed into the normal $\vec{F}^n$ and shear (tangential) $\vec{F}^t$ directions, as it is schematically shown in

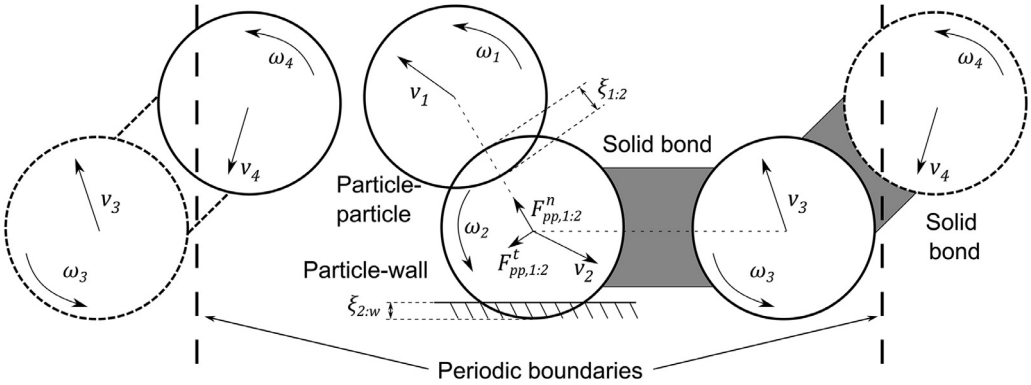

Fig. 3. Schematic illustration of three types of interaction models in the presence of periodic boundary conditions.

Fig. 3 ($\vec{F}^{n}_{pp,1:2}$, $\vec{F}^{t}_{pp,1:2}$). The total force acting in particle-particle contact is calculated as the sum of normal and tangential components according to Hertz-Mindlin model [44,66] as:

$$\vec{F}^{n}_{pp,i:j} = \hat{u}_n \frac{4}{3} E^* \cdot \sqrt{\left(\xi^{n}_{i:j}\right)^3 \cdot R^*} - 1.83 \cdot \alpha \cdot \vec{v}^{n}_{rel,i:j} \sqrt{2E^* \cdot \left(\xi^{n}_{i:j}\right)^{0.5} \cdot m^*} \tag{5}$$

$$\vec{F}^{t}_{pp,i:j} = 8\vec{\xi}^{t}_{i:j} \cdot G^* \cdot \sqrt{\xi^{n}_{i:j} \cdot R^*} - 3.66 \cdot \alpha \cdot \vec{v}^{t}_{rel,i:j} \sqrt{2G^* \cdot \left(\xi^{t}_{i:j}\right)^3 \cdot m^*} \tag{6}$$

Here m^*, E^*, G^*, and R^* are the equivalent mass, Young's modulus, shear modulus, and radius in this contact, respectively; ξ^n and $\vec{\xi}^t$ are the normal and tangential overlaps; $\hat{u}_n$ is the unit vector in normal direction, α is a parameter calculated depending on the restitution coefficient (e), which defines the amount of dissipated kinetic energy.

$$\alpha = \frac{\ln(e)}{\sqrt{\pi^2 + \ln^2(e)}} \tag{7}$$

The relative velocities at the contact point in the normal $\vec{v}^{n}_{rel}$ and tangential directions $\vec{v}^{t}_{rel}$ are calculated based on the translational ($\vec{v}$) and rotational velocities ($\vec{\omega}$) of the contact partners. The normal overlap ξ^n is calculated directly based on the current positions of particles. The calculation of tangential overlap $\vec{\xi}^t$ is performed in the iterative manner, considering slipping condition and motion of particles in three-dimensional space. In each simulation time step the old tangential overlap is updated considering relative motion in the previous time step. Afterwards, the resulting elastic component of tangential force is computed according to Eq. (8) and the slipping condition given in Eq. (9) is analyzed.

$$\vec{F}^{t,el}_{pp,i:j} = 8\vec{\xi}^{t}_{i:j} \cdot G^* \cdot \sqrt{\xi^{n}_{i:j} \cdot R^*} \tag{8}$$

$$\left|\vec{F}^{t,el}_{pp,i:j}\right| \leq \mu_{sl} \cdot \left|\vec{F}^{n}_{pp,i:j}\right| \tag{9}$$

If the condition is not satisfied, then the magnitude of the elastic part of the tangential force is limited by the magnitude of the normal force multiplied by the sliding friction coefficient (μ_{sl}). In this case, the tangential displacement is updated based on the new value of the tangential force as:

$$\vec{\xi}^{t}_{i:j} = \frac{\vec{F}^{t,el}_{pp,i:j}}{G^* \cdot \sqrt{\xi^{n}_{i:j} \cdot R^*}} \tag{10}$$

The rotational moments induced by particle-particle or particle-wall interactions are calculated based on the tangential force considering additional rolling resistance.

The relative motion of particles connected by a solid bond causes the formation of normal and tangential forces acting on particles, as well as torsional and bending moments. The forces are calculated according to the ideally elastic model [14,50]:

$$\begin{aligned} F_{b,i:j} &= \left[\vec{F}^{n}_{b,i:j}\right] + \left[\vec{F}^{n}_{b,i:j}\right] \\ &= \left[\frac{L_{b,i:j} - L^{init}_{b,i:j}}{L^{init}_{b,i:j}} E_b \cdot A_{b,i:j}\right] + \left[\vec{\xi}^{t}_{b,i:j} \frac{E_b \cdot A_{b,i:j}}{2 \cdot L^{init}_{b,i:j}\left(1+\nu_b\right)}\right] \end{aligned} \tag{11}$$

where E_b and ν_b are the Young's modulus and Poisson's ratio of the bond material; A_b is the bond's cross-cut surface; L^{init}_b and L_b are the initial and current bond length; $\vec{\xi}^{t}_{b}$ is the bond deformation in tangential direction. The bond deformation in the normal direction can be directly calculated based on the actual position of particles. However, $\vec{\xi}^{t}_{b}$, as in the case of particle-particle contact, is calculated incrementally:

$$\vec{\xi}^{t}_{b,i:j}(t+\Delta t) = T_{i:j} \cdot \vec{\xi}^{t}_{b,i:j}(t) + \Delta t \cdot \vec{v}^{t}_{rel,i:j} \tag{12}$$

Here T is the rotational matrix calculated to consider the motion of connected particles. In vector notation ($\vec{u} = \{u_x, u_y, u_z\}$) it is defined as:

$$\vec{\phi} = \vec{r}_{i,j}(t+\Delta t) \cdot \left[\left(\vec{\omega}_i + \vec{\omega}_j\right) \cdot \vec{r}_{i,j}(t+\Delta t)\right] \cdot \frac{\Delta t}{2} \tag{13}$$

$$\vec{q} = \vec{r}_{i,j}(t) \times \vec{r}_{i,j}(t+\Delta t) \tag{14}$$

$$T_{i,j} = \begin{pmatrix} +q_z \cdot \phi_z + q_y \cdot \phi_y & \phi_z - q_z - q_y \cdot \phi_x & -\phi_y - q_z \cdot \phi_x + q_y \\ q_z - \phi_z - q_x \cdot \phi_y & q_z \cdot \phi_z + 1 - q_x \cdot \phi_x & -q_x \cdot \phi_y + \phi_x - q_x \\ -q_y - q_x \cdot \phi_z + \phi_y & -q_y \cdot \phi_z + q_x - \phi_x & q_y \cdot \phi_y + q_x \cdot \phi_x + 1 \end{pmatrix} \tag{15}$$

where $\vec{r}_{i,j}$ is the unit vector connecting the centers of the particles.

At each simulation time step, the stresses acting in each single bond are calculated and compared to their normal σ_{max} and tangential τ_{max} strengths. If the stresses in a particular bond exceed the material strength, the bond is considered broken. If $I_{i:j}$ and $J_{i:j}$ are the moment of inertia and the polar moment of inertia of the bond's cross-section, respectively, and $R_{b,i:j}$ is the bond radius, the breakage conditions can be formulated as follows:

$$\frac{\left|\vec{F}^{n}_{b,i:j}\right|}{A_{b,i:j}} + \frac{\left|\vec{M}^{n}_{b,i:j}\right| \cdot R_{b,i:j}}{I_{i:j}} < \sigma_{max} \tag{16}$$

$$\frac{\left|\vec{F}^{t}_{b,i:j}\right|}{A_{b,i:j}} + \frac{\left|\vec{M}^{t}_{b,i:j}\right| \cdot R_{b,i:j}}{J_{i:j}} < \tau_{max} \tag{17}$$

The proposed model does not consider the interaction between particles connected with a solid bond. Consequently, in situations where the solid bond is broken and the bond is therefore removed from the scene, a large interparticle force can arise spontaneously. To avoid possible instabilities, a time-dependent relaxation of the bond has been included.

If at least one of the bond fracture conditions is met, the bond is marked as broken, however it is not instantaneously removed from the calculations, but remains active for a short period of time (1 ns). During this period, the normal and tangential stiffnesses of the bond are decreased at a rate of 1% in 10^{-11} s.

Using the BPM calculation approach is computationally expensive. This is caused by a large number of simulated objects and a small modelling time step. To overcome this problem, a hybrid CPU-GPU computational technique was developed and implemented in the open-source simulation framework MUSEN. The contact detection was performed on the CPU applying the linked-cell method [52], Verlet lists [67] and multigrid approaches [29]. During modelling, a list is generated, which contains not only contacts that are active in the current time point, but also potential contacts which can occur within a specific time slot. This allows integration of motion and computation of interactions on a graphics processing unit (GPU) without transferring data between the CPU and the GPU after each simulation step. When the periodic boundary conditions are enabled, the list of potential contacts is extended by particle-particle or particle-wall interactions that can occur over boundaries. Moreover, the solid bonds can be directly created across PBC.

The implemented code was parallelized on the CPU according to the shared memory model. For the parallelization of computations on the GPU the CUDA computing platform was used.

3. Behavior of ideally ordered structures

3.1. Uncoated SiO_2 samples

3.1.1. Convergence analysis

Selection of the appropriate simulation domain is crucial when modeling heterogeneous materials, since it determines the accuracy and representativeness of the structural model. In most cases, a representative volume element (RVE) is defined [4], and simulation is performed using suitable boundary conditions. On the one hand, the size of the RVE must be large enough to contain sufficient information about the microstructure. On the other hand, it should be much smaller than the macroscopic body [18,27]. Often, to simulate ideally ordered periodic structures, it is sufficient to use the domains containing one single unit cell [57,59]. However, to analyze the influence of stacking faults, which lead to non-ideally ordered structures, a much larger size of simulation domain should be used.

With respect to boundary conditions, three different configurations, which satisfy Hill-Mandel condition, are usually distinguished [40]: periodic boundaries, affine displacement and stress boundaries. In the scope of this work, periodic boundary conditions and open boundaries were used. Here, the combination of centric or eccentric positioning of inclusions with specific boundary conditions can influence the stress distribution [59]. For ideally ordered FCC structures, we applied a centric arrangement of pores with symmetry at the axial boundaries. The size of the final simulation domains was relatively large, so the influence of positioning was minimized.

To ensure that the size of the modeled sample is large enough to correctly represent the material behavior, the influence of the simulation domain was first analyzed. For this purpose, structures of various geometric sizes were investigated: the area of the cross-sectional surfaces of the samples varied from 1 to 15.1 μm^2, and the height was 2.01 or 2.63 μm, which corresponded to three and four vertical pore layers, respectively. The step size over the sample area was limited by the need for the correct structural patterns at the boundaries with periodic boundary conditions. In Fig. 4, two exemplary samples with different volumes ordered according to a face-centered cubic (FCC) lattice are shown.

The mechanical behavior of samples was investigated by simulating uniaxial compression tests. The model parameters used for these calculations are described in the next chapter. As a result, based on the obtained force-displacement characteristics, Young's modulus and compressive strength were calculated for all pieces. It should be noted that the simulation results can be affected not only by the size of the sample, but also by the random placement of primary particles in the initial packages caused by the generation procedure described in the previous section. Therefore, in order to take this into account, three samples of each size were generated and analyzed. From the results shown in Fig. 5, it can be seen that for all samples whose cross-sectional area exceeds 4 μm^2, the size of the sample has a minimal effect, and the deviations are less than 0.12% for Young's modulus and 4% for compressive strength. Maximum deviations caused by random placement of particles in these larger samples are 0.16% and 6.5%, respectively. Finally, a comparison of samples consisting of 3 and 4 layers shows that thinner structures have a slightly higher Young's modulus. However, this difference can be neglected, since the experimental range of Young's modulus obtained by do Rosário et al. [57] is 10 times lager. In order to reduce computational effort, only samples with a height of 2.01 μm and a cross-sectional area of 8.05 μm^2 were used for further studies.

Since the discrete element method is based on an explicit integration scheme, the selection of a suitable simulation time step is crucial for the correctness and accuracy of the simulation results [7,64]. Due to the very stiff materials and the small size of the primary particles, a time step of 10^{-12} s was used in all case studies.

3.1.2. Model parameters identification

One of the main challenges associated with the use of BPM is an adjustment of unknown model parameters. Since, there is always some deviation between the real material microstructure and its BPM representation, even with exact knowledge about the material properties, calibration of the model is needed. The most widely used calibration strategies are based on inverse analysis principle with application of different methods for design of experiments [14,23,60,72]. More advanced strategies, like proposed by Estay et al. [19] or the linearization-based method used by Jarolin et al. [31], allow to estimate the model parameters directly based on the structural model. However, since the developed BPM model has a relatively small number of unknown parameters, the relatively simple parameter identification procedure was applied in this work. The model parameters, namely Young's modulus of bonds E_b (s. Eq. (11)) as well as their normal σ_{max} and tangential τ_{max} strengths (s. Eqs. (16) and (17)) were varied and their influence on force-displacement characteristic was analyzed. Based on the deviations between experimental data and simulation results and using iterative Newton's optimization approach, an optimal parameter set was identified.

The algorithm for identifying the values of the required parameters worked as follows. In all case studies it was assumed that the normal and tangential strengths of the solid bonds' material are equal. Therefore, only two parameters were varied: Young's modulus $E_{b,i}$ and strength $\sigma_{max,i}$. From the results of the DEM simulations, the force-displacement characteristic was extracted and the Young's modulus $E_{DEM,i}$ and the compressive strength $\sigma_{DEM,i}$ of the porous structure were obtained. The strength was calculated based on the maximum force, and the Young's modulus was determined assuming a linear slope of the stress-strain diagram. Finally, the obtained results were compared with the experimental data (E^* and σ^*). Based on the discrepancy between these values, the parameters for the next simulation were calculated, as it is shown for the Young's modulus in Eq. (18). Breakage strength was calculated in a similar way.

$$E_{b,i+1} = E_{b,i} + \frac{E^* - E_{DEM,i}}{\frac{\partial E_{DEM,i}}{\partial E_{b,i}}} \tag{18}$$

The derivative $\partial E_{DEM,i}/\partial E_{b,i}$ was calculated with finite difference approximation as:

$$\frac{\partial E_{DEM,i}}{\partial E_{b,i}} = \frac{\hat{E}_{DEM,i} - E_{DEM,i}}{\Delta E_b} \tag{19}$$

Where ΔE_b is a small perturbation step in $E_{b,i}$, and $\hat{E}_{DEM,i}$ is the Young's modulus of the sample extracted from DEM calculations us-

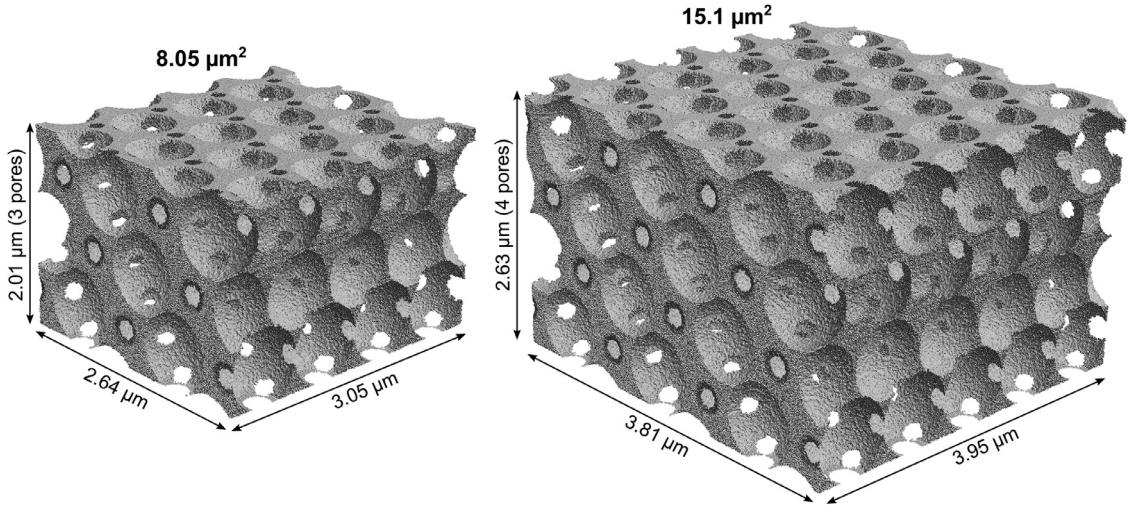

Fig. 4. Uncoated SiO2 inverse opals of different sizes.

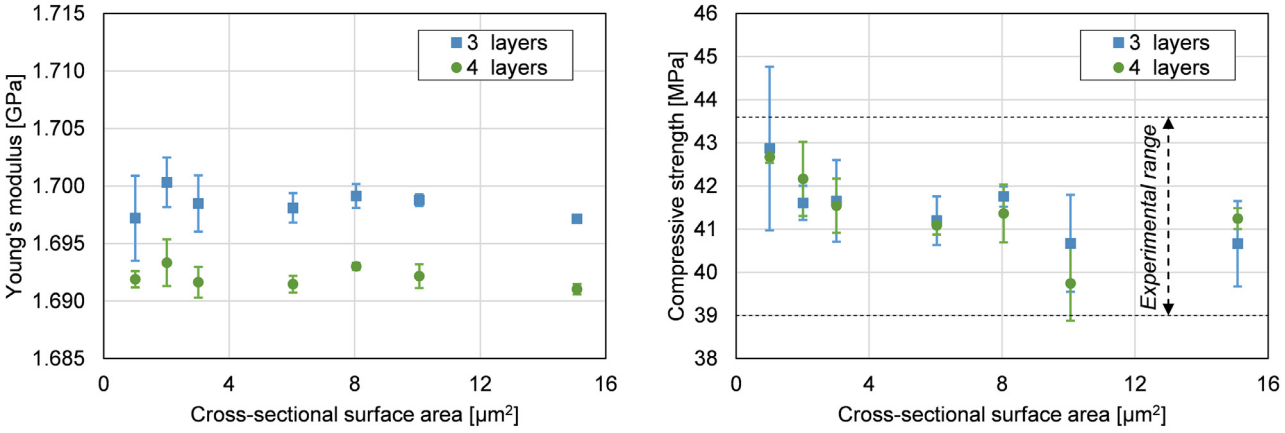

Fig. 5. Influence of sample size on the mechanical response.

ing the Young's modulus of bonds equal to $E_{DEM,i} + \Delta E_b$. The iterations were repeated until the difference between the desired value E^* and the DEM model $E_{DEM,i}$ reached 0.5%. It worth noting that during the iterative search it was assumed that the strength of the bonds does not affect the Young's modulus of the sample $\partial E_{DEM,i}/\partial \sigma_{max,i} = 0$ and the Young's modulus of bonds has no influence on the strength of the modeled sample $\partial \sigma_{DEM,i}/\partial E_{b,i} = 0$.

The stiffness and the strength of uncoated silica samples obtained from experimental results of do Rosário et al. [57] were used to calibrate unknown model parameters: Young's modulus of particles and solid bonds and fracture strength of bonds. Calibration results showed that for the proposed structural model, the Young's modulus of silica particles and bonds should be equal to 6.53 GPa, and the fracture strength should be 94.3 MPa. In this case, the porous structure consisting of 3 layers (2.01 μm) and having a cross-sectional surface area of 8.05 μm^2 reveals a Young's modulus of 1.7 GPa and a compressive strength of 41.1 GPa. These values are in good agreement with the experimental data of 1.7 ± 0.1 GPa and 41.3 ± 2.3 GPa, respectively [57].

Another important parameter is the scaling factor K_E, which characterizes the relationship between the microscale model parameters (Young's modulus of primary particles and bonds) and the material properties at the macroscale. It is defined as:

$$K_E = E_{macro}/E_b \tag{20}$$

where E_{macro} is the macroscopic Young's modulus of a monolithic sample obtained from the BPM computations. Due to the linear elastic model of solid bonds, it can be assumed that K_E is constant and it depends only on the structural model (packing of primary particles and their connectivity with solid bonds). This assumption allows to directly estimate the Young's modulus of bonds E_b for known material.

To compute the scaling factor for the proposed packing generation algorithm, a silica sample was generated without macropores, and its stiffness was determined using the uniaxial compression test. The numerically determined Young's modulus of such a bulk silica sample E_{macro} = 21.9 GPa and corresponds to the scaling factor for the proposed structural model of K_E = 3.35. The Young's modulus of 21.9 GPa is comparable to the value of 17.52 GPa obtained from the FEM-based calibration performed by do Rosario et al. [57]. The corresponding fracture strength of the bulk silica is 601 MPa, which is approximately $E_{macro}/35$ and in the range $[E_{macro}/\pi\ , E_{macro}/35\ ]$ of the estimates for the predictions of the theoretical strength of a perfect material [20,46,49].

An overview of all the model parameters used in simulations is given in Table 1. In the first column the model parameters used for BPM computations are listed. In the second column the resulting material parameters are shown. These are the properties of monolithic silica or titania samples represented with the corresponding BPM model.

3.1.3. Mechanical behavior

The compression of the inverse opals leads to heterogeneous deformations occurring in the different zones, such as struts or nodes. In order to characterize these zones, the deflection of bonds in the normal direction was analyzed. The normal direction is the vector between

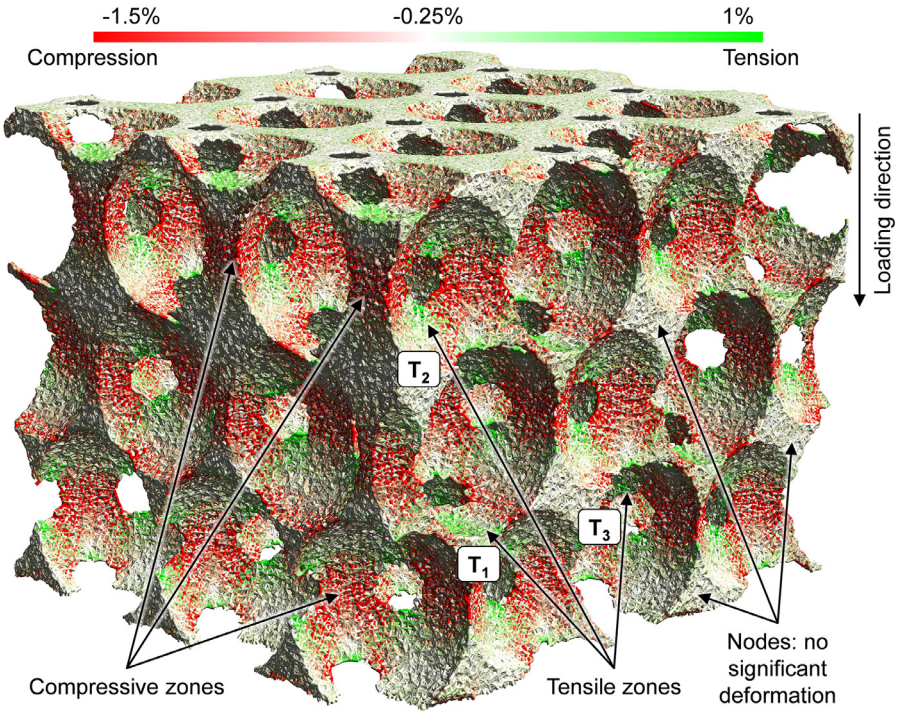

Fig. 6. Localized deformation of bonds in the silica sample at macroscopic strain of 2%.

Table 1
The main BPM model parameters and the corresponding material properties of a perfect monolithic material

Parameter	BPM model parameters	Material properties (perfect monolithic material)	Units
Silica			
Young's modulus	6.53	21.9	GPa
Poisson ratio	0.17		-
Fracture strength	94.3	601	MPa
Titania			
Young's modulus		(experiments [11])	GPa
10 nm	13.72±8.35	46.0±28	
20 nm	17.89±5.37	60.0±18	
32 nm	22.21±4.47	74.5±15	
Poisson ratio	0.28		-
Fracture strength	834	2843	MPa

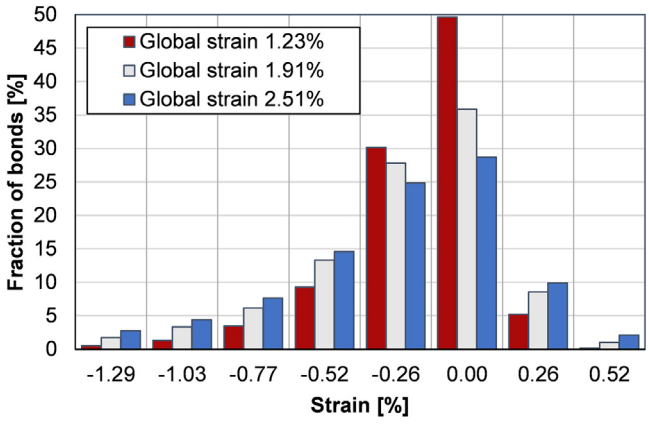

Fig. 7. Deformation of an uncoated sample: distribution of solid bonds over strains for three different compression stages.

the centers of the connected particles. In Fig. 6, the deflection of the bonds for instantaneous time point, where the overall (global) strain was equal to 2%, is shown. Here, the solid bonds are colored according to their strains. Positive values represent tension, and negative values represent compression. From the results obtained, it can be seen that the largest compressive deformations occur at the regions of the struts in the loading direction. At the same time, the tensile zones are built near the interpore openings. On the one hand, they are formed above and below the pores (T_1 in Fig. 6). On the other hand, they can be found in the interpore holes oriented parallel to the direction of loading (T_2 and T_3). The material situated in the nodes undergoes only insignificant deformations.

The loading-dependent deformation of single bonds at the three stages of deformation is shown in Fig. 7. It can be seen that the largest fraction of bonds has negative strain that means they are compressed. When the macroscopic strain of the sample is equal to 1.23%, only 5% of bonds have an average elongation of 0.26%. In the same time, the number of shortened bonds in the same range of values is about 31%. Moreover, it can be seen that with an increase in the overall strain from 1.23% to 2.51%, the distribution becomes wider, which indicates larger inhomogeneity of the localized deformations. Such inhomogeneity can be also visually observed in Fig. 6.

The bonded particle method allows to explicitly consider material fracture, starting with the initiation of initial defects, continuing with the propagation of cracks and their coalescence, and ending with the overall fracture of the sample. Fig. 8 shows two fracture patterns for uncoated silica sample consisting of 4 layers of pores with a cross-sectional area of 8.05 μm^2. Since, the periodic boundary conditions significantly influence the breakage behavior, the fracture patterns with periodic boundaries and with open boundaries were investigated and compared. In the both cases, initial defects and cracks originate starting from the interpore openings. In the presence of PBC, the longitudinal cracks are formed in the sample, perpendicular to the loading direction: in Fig. 8.b, one macroscopic crack passing through the entire sample can be observed. Contrary to this, in the sample with open boundaries (Fig. 8.a), vertically oriented intrapore cracks are formed.

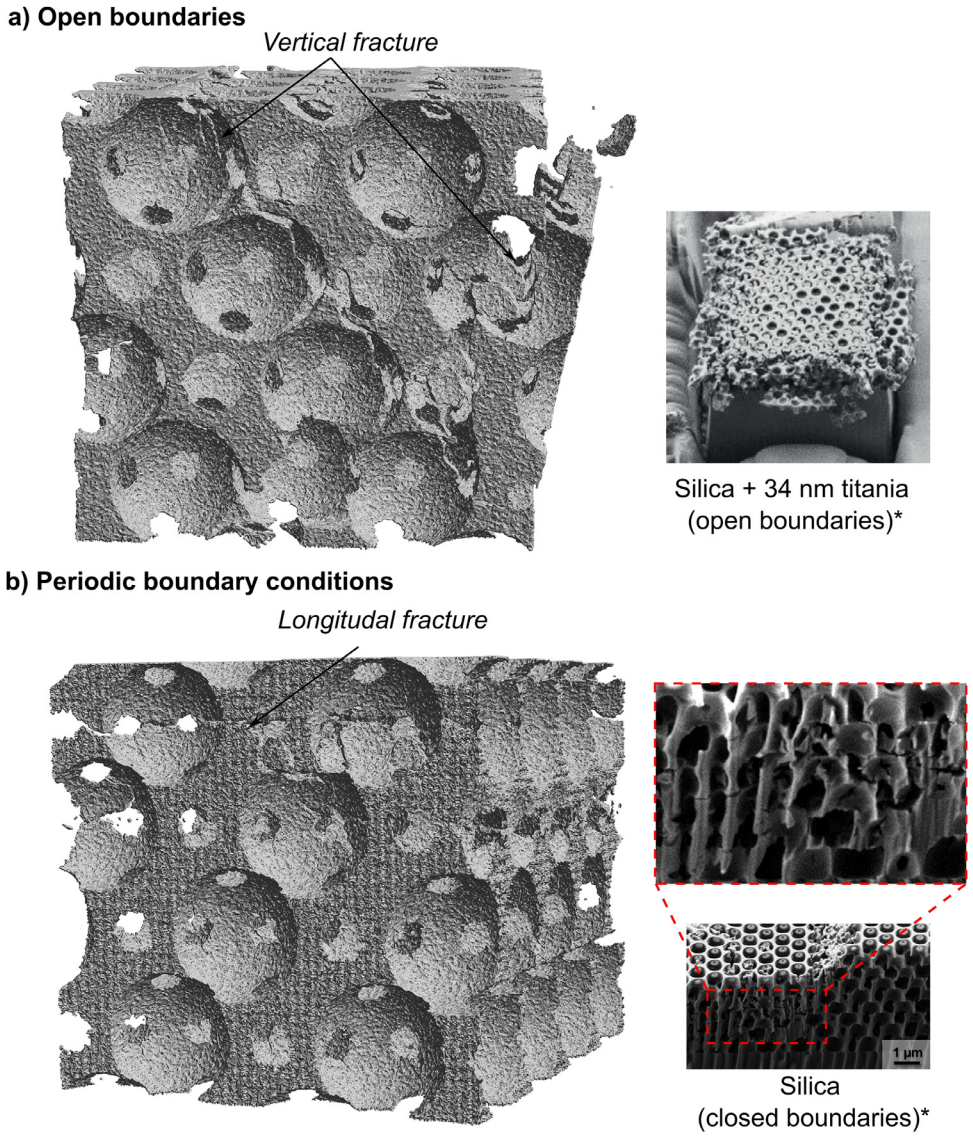

Fig. 8. Fracture patterns observed in simulation and experiments for (a) open and (b) closed boundaries. a) Simulation results of an uncoated sample and a SEM image for silica coated with 34 nm TiO2; b) Simulation results of an uncoated silica sample with PBC and SEM image for flat punch indentation for uncoated sample. *SEM images reprinted from do Rosario et al., 2020 with permission from Elsevier.

3.2. Coated structures

To further validate and analyze the applicability of the proposed model under different scenarios, modelling of coated structures was carried out. The inverse opals of SiO_2 were coated with TiO_2 layers of three different thicknesses: 10, 20 and 34 nm. In this case, no further calibration of the titania's Young's modulus was necessary, since experimentally measured values from Colombi et al. [11] are available. For the three thicknesses (10, 20 and 34 nm) of TiO2 the following Young's moduli were taken respectively: 46±28 GPa, 60±18 GPa and 74.5±15 GPa (Colombi et al. [11]). After that, the model parameters of titanium dioxide bonds were recalculated using the scaling factor of 3.35 from Eq. (20). Thus, for each thickness, three different values of Young's modulus were obtained by using either the experimental mean value or the mean value plus or minus the standard deviation. For example, samples with a thickness of 10 nm TiO_2 were modeled using the values (46 - 28) / 3.35 = 5.37, 46 / 3.35 = 13.72 and (46 + 28) / 3.35 = 22.07 GPa (see Table 1). This made it possible to consider the values from the region of standard deviations observed in the experimental measurements. For all case studies, the strength of single bonds of TiO_2 was calibrated to be 834 MPa, which corresponds to the total strength of a monolithic sample of titania of 2.84 GPa (Table 1), which is in the range of theoretical predictions [20,46,49].

In Fig. 9, the Young's moduli and compressive strengths obtained from the performed BPM simulations, as well as their comparison with the experimental data and the results from FEM simulations (both from [57]) are illustrated. As expected, due to the higher stiffness and strength of titania, an increase in a coating layer allows to significantly improve mechanical properties. A comparison between numerical results and experimental data shows that after adjusting the titania strength for a layer of 10 nm, the proposed model is able to predict compressive strength for thicknesses of 20 and 34 nm with high accuracy. The deviations between experimental and numerical results for a thickness of 34 nm is less than 2.2%. However, there are large deviations for the Young's modulus: the BPM model used underestimates the stiffness for thin layers and overestimates it for the 34 nm TiO_2 layer. Similar deviations were also observed in previous FEM simulations [57].

In Fig. 10 the typical stress-dependent mechanical behavior of material obtained from BPM simulation and from experiments of do Rosário et al. [57] are shown. In this figure the results for a silica sample coated with 20 nm titania layer are demonstrated. The simulation was performed using the upper estimation of Young's modulus for titania of 78 GPa [11].

Analyzing the results, one can notice that both curves which represent Young's modulus reveal similar behavior and in both three main regions can be distinguished. In the first region, an initial contact is

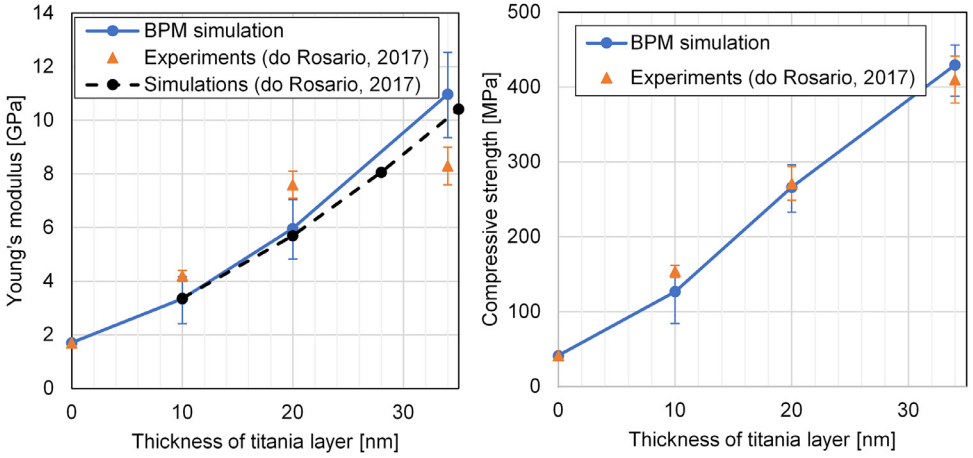

Fig. 9. Dependency of stiffness and compressive strength on the coating thickness of inverse silica opals with titania coating.

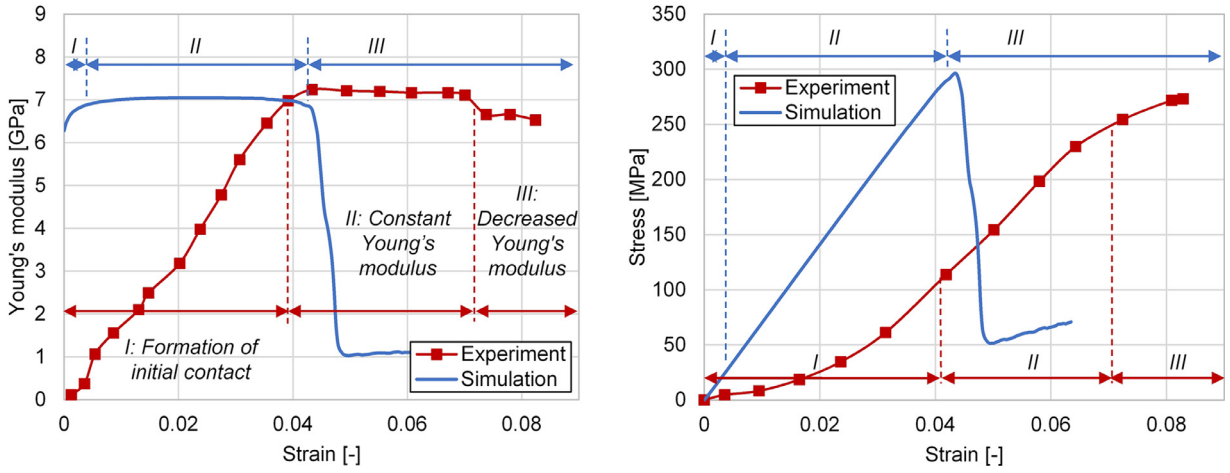

Fig. 10. Dependency of Young's modulus on strain and stress-strain diagram for a silica sample coated with 20 nm titania layer. The experimental data from do Rosário et al. [57].

formed, and the estimated Young's modulus increases. After that, in the second region, the Young's modulus has an almost constant value, which subsequently decreases in the third region due to the fracture or plastic deformations occurring in the material. However, unlike a virtual sample, experimental samples do not have an ideally flat surface with perfectly oriented pores. As a result, the region of the initial contact formation in the experiments is about 4% of strain, that is much larger compared to approximately 0.5% in the simulation. The shift of the curves by the strain difference shows that simulation results are in good agreement with the experimental data. However, it should be noted that here the material already reveals elasto-plastic behavior, which is not considered by the DEM simulation, since the ideally elastic model of solid bonds is employed. As a consequence, this leads to a mismatch in the slope of the stress-strain diagram shown on the right-hand side in Fig. 10.

The second important difference is the material behavior in the third region, where material fracture and plastic deformation occur. In this work, a simplification was made, and single solid bonds for silica and titania were modeled with purely elastic rheological model (Eq. (11)), without consideration of plasticity. As a consequence, the differences in the material behavior in the third region can be observed. A similar shift in values caused by a non-flat surface can be observed also in the stress-strain diagram.

The three highlighted regions in Fig. 10 should not be confused with those ones that are typically distinguished in the stress-strain diagrams of highly-porous materials, namely: elastic, plastic plateau and densification. In this contribution we only focus on the initial elastic region with the relative low strains.

To compare the effect of the coating layer on the distribution of stresses within the structure, the Cauchy stress tensor for primary particles was calculated as [65]:

$$\sigma_{i,j} = \frac{1}{2V_p} \sum_{K} l_i \cdot F_j \tag{21}$$

where K is the total number of contacts, F are the forces acting in each contact, l is the branch vector, and V_p is the volume of particles. It should be noted that when using BPM, solid material appears as a set of non-overlapping spherical particles. This leads to an artificial porosity, which means that the total volume of all particles $\sum^{V_p}$ is smaller than the volume of the modeled object. As a consequence, the use of the correlation given in Eq. (21) leads to an overprediction of the absolute values of stresses. However, it can be effectively used to compare structures or to analyze the influence of different parameters.

Fig. 11 and Table 2 show the results of the analysis of stresses acting on the primary particles of different materials in a pure silica sample and in a sample coated with a titania layer of 20 nm. The stresses acting in the vertical (loading) direction (σ_{zz}) and in the axial direction (σ_{xx}) are illustrated there. These values are the two diagonal elements of Cauchy stress tensor (s. Eq. (21)). Negative values correspond to the compressive stress and positive values to the tensile stress. Fraction in Fig. 11 is the number of particles of a specific material divided by the total number of particles. The overall compressive stress for both samples was equal to 31.3 MPa.

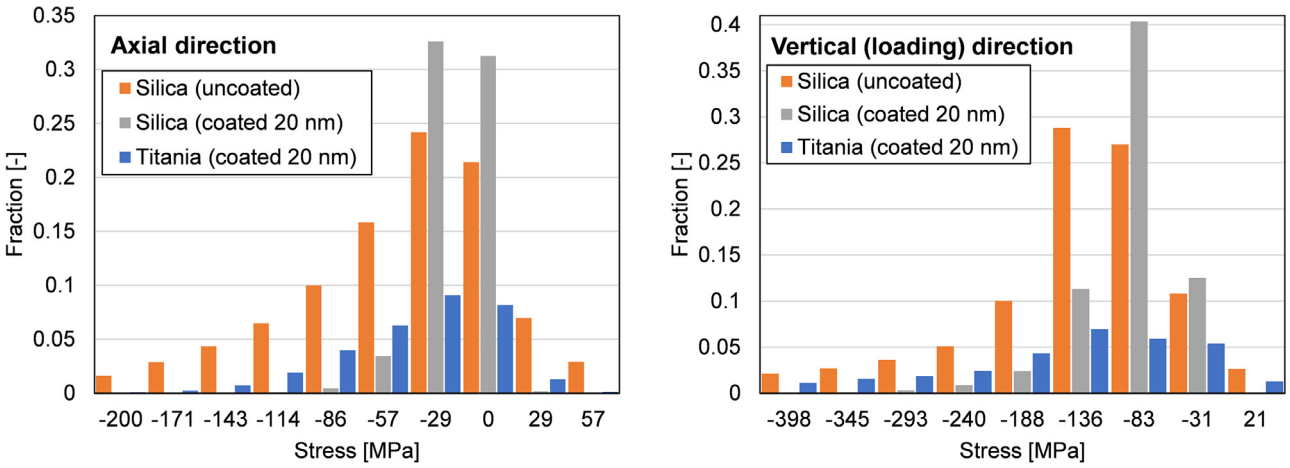

Fig. 11. Distribution of stresses acting on particles in uncoated and coated (20 nm titania) structures. Negative values represent compressive stresses, positive values represent tensile stresses.

Table 2
Average compressive stress in the axial (σ_{xx}) and vertical (σ_{zz}) irections in a sample coated with 20 nm of titania.

	Silica		Titania	
	σ_{xx} [MPa]	σ_{zz} [MPa]	σ_{xx} [MPa]	σ_{zz} [MPa]
Uncoated	44.5 ± 63.2	162.8 ± 135.3	-	-
Coated	18.1 ± 14.9	88.9 ± 44.32	40.88 ± 42	158 ± 121.2

From the obtained results several conclusions can be drawn:

- Prevailing compressive stresses act in the axial direction, and there are almost no tensile stresses in the loading direction.
- Regardless of the type of material, the average axial stress is roughly four times smaller than the vertical stress.
- The TiO_2 coating layer with a thickness of 20 nm allows to reduce stresses acting on silica by almost half. The average stresses in the loading direction for samples with and without coating are 88.9 and 162.8 MPa accordingly.
- The inverse opal structure has a large inhomogeneity in the distribution of stresses. Standard deviations are almost in the range of 100%. Adding a coating layer allows to slightly homogenize the stress distribution in silica under load.

The spatial distribution of σ_{yy} and σ_{zz} stresses for uncoated sample and material coated with 20 nm titania are shown in Fig. 12. Here the continuous representation of stresses is shown for three orthogonal planes. To convert discrete data obtained from the DEM simulation to the continuous view, linear interpolation in 3D space were performed using MATLAB package with *scatteredInterpolant()* function. Since the compressive stresses prevailing in the structure, the selected colormap limits for tensile stress were four times smaller than for compressive. Moreover, the limits were selected not based on the maximum value on stresses, but to have clear representation of stresses distribution.

It can be observed that the both samples have significant differences in stress patterns. In the coated structures the largest part of the load is absorbed by the titania shell and the magnitude of stresses in the silica is much smaller compared to the uncoated sample. Similar results from FEM computations were reported by do Rosário et al. [57]. Moreover, the axial stress σ_{yy} is non-homogeneously distributed on the pores' surfaces forming compressive and tensile zones. The largest gradients of vertical or axial stresses are formed near the interpore openings. This directly correlates with the fracture pattern (Fig. 8), where the initial cracks formation was observed near the interpore openings.

4. Disordered structures with varied porosities

The overall porosity of the final structure, the shape of the pores, their orientation and ordering have a crucial influence on the mechanical behavior of the material. Various correlations exist to describe the relationship between porosity and the mechanical properties of ceramics [53]. One of the widely applied correlations between Young's modulus and porosity for spherical pores is the exponential function given in Eq. (22) [1,25,62]:

$$E(\epsilon) = E_0 \cdot e^{-b\cdot\epsilon} \tag{22}$$

Here, E is the Young's modulus of the porous material, E_0 is the elastic modulus of the non-porous material, ϵ is the porosity, and b is an empirical parameter. The parameter b strongly depends on the type of material and typically varies in the range between 2.2 and 4.5 [53]. Another correlation for describing the dependence of Young's modulus on the open porosity in ceramics was proposed by Wagh et al. [68] and it can be expressed as

$$E(\epsilon) = E_0 \cdot (1-\epsilon)^m \tag{23}$$

where m is the exponential parameter, which depends on the tortuosity of the ceramic structure.

To analyze the influence of porosity on mechanical behavior, several samples were generated with a different number of pores, and hence with different porosities, using the algorithm described above. A total of six different porosities were analyzed. Since the initial random arrangement of pores can affect the mechanical properties of the material, five samples for each porosity were generated. In Fig. 13, two final exemplary structures with porosities of 63% and 39% are shown. It should be noted that a decrease in porosity leads to an increase in computational effort. Therefore, the minimum porosity in this study was limited by computational complexity and, thus, the simulation time. The samples with 39% porosity consist of about 3.4 million particles and 39.4 million solid bonds.

In Fig. 14.a, the dependencies of the compressive strength and the Young's modulus on the porosity obtained from the simulation results are shown. The both characteristics decrease with higher porosities. An increase in porosity from 0.49 to 0.63 leads to an almost two-fold decrease in the average Young's modulus from 6.3 to 3.3 GPa and the compressive strength from 92.9 to 46.7 MPa.

The dependency of Young's modulus on the porosity was approximated by correlations given in Eqs. (22) and (23). For this purpose, the parameters b and m were adjusted to the BPM simulation results, and thus correlations Eqs. (24) and (25) were obtained: the parameter b in the exponential function was evaluated to 2.99 and parameter m from

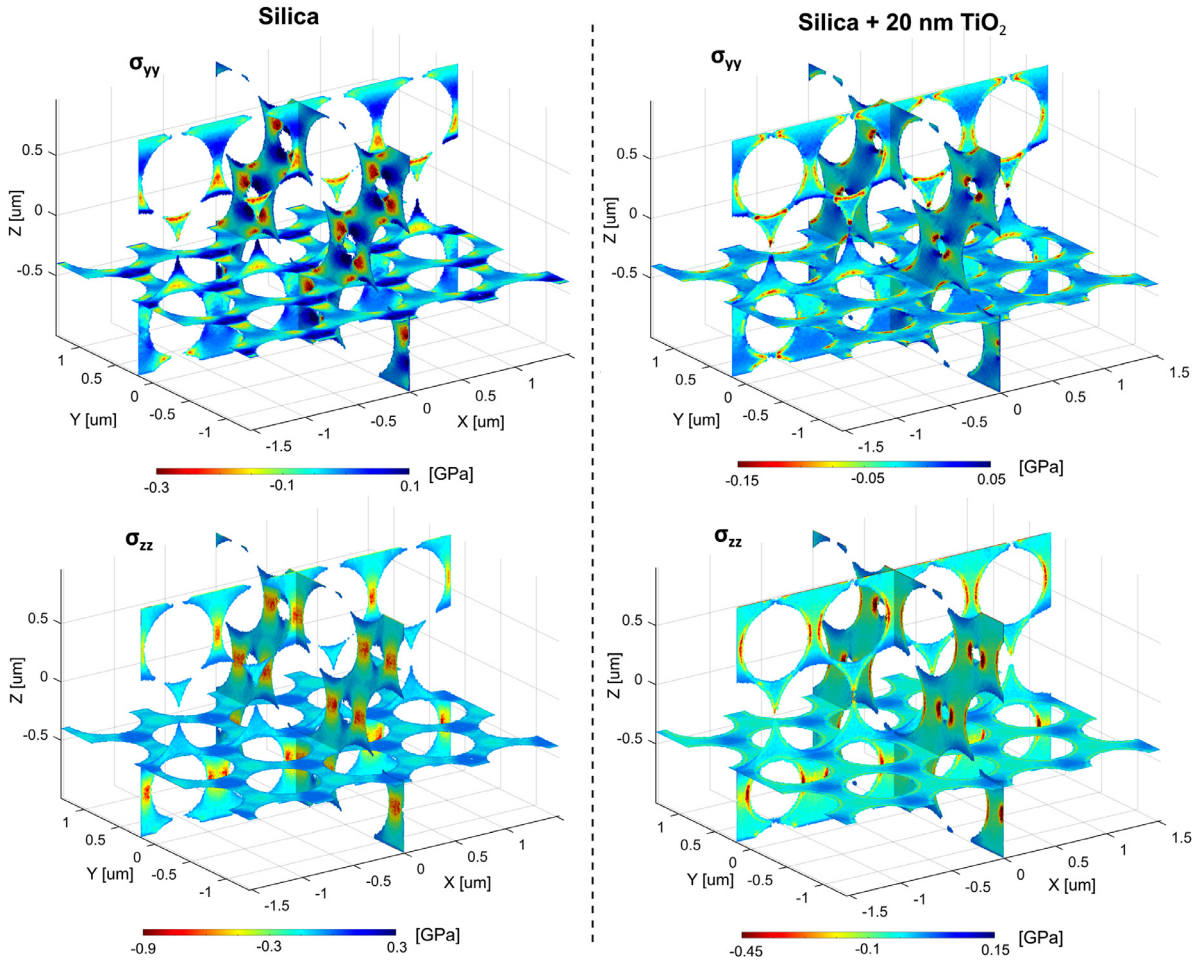

Fig. 12. Spatial distribution of stresses acting on particles in uncoated and coated (20 nm titania) structures. Stresses are shown for three orthogonal slices. Negative values represent compressive stresses, positive values represent tensile stresses. The overall compressive stress for both samples was equal to 31.3 MPa.

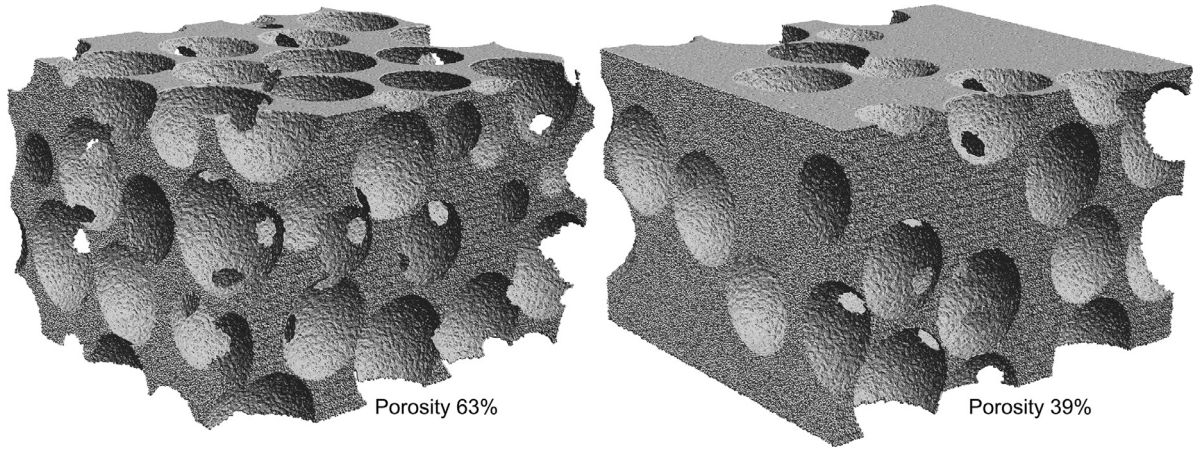

Fig. 13. Two exemplary samples with different porosities.

the correlation of Wagh et al. [68] – to 1.92. In their work, Wagh et al. [68] showed that for sintered ceramic m has a value of nearly 2. However, it was found that the exponential correlation from Eq. (22) leads to a large discrepancy and cannot effectively represent the simulation results. At the same time, the function in Eq. (25) almost perfectly describes the obtained dependency of Young's modulus on porosity.

$$E_{macro} = 22.06 \cdot e^{-2.99 \cdot \varepsilon} \tag{24}$$

$$E_{macro} = 22.06 \cdot (1 - \varepsilon)^{1.92} \tag{25}$$

The exponential relation (26) is suitable to describe the dependency between the porosity and the compressive strength [53]. Here, the exponential factor b is almost equal to 4. It can be also observed, that the FCC structure with 74% porosity does not completely follow the descending trend. The compressive strength of the structure, which is 41.76±0.24 MPa, is higher than the value predicted with Eq. (26). This is due to

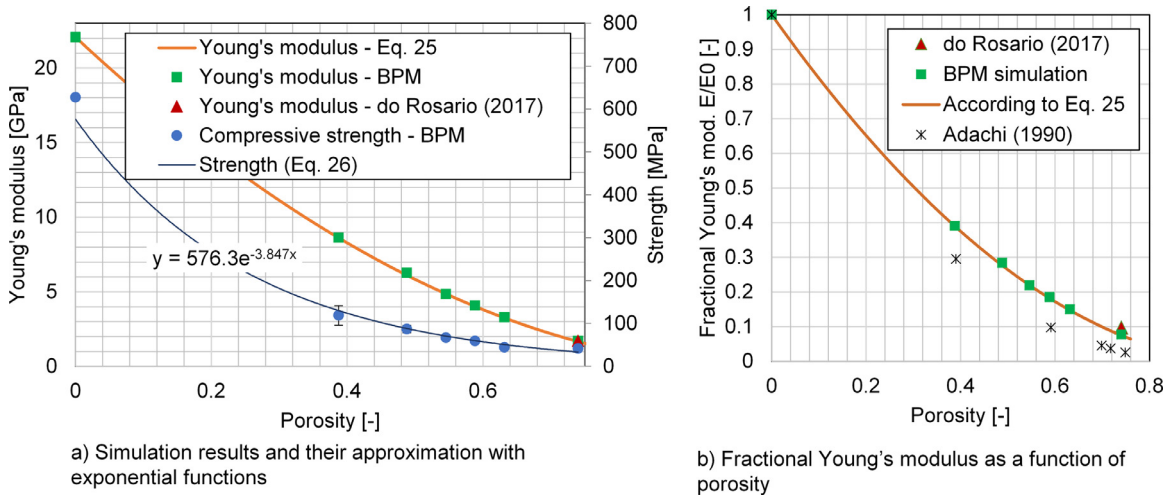

Fig. 14. Dependency of Young's modulus and strength on the packing porosity.

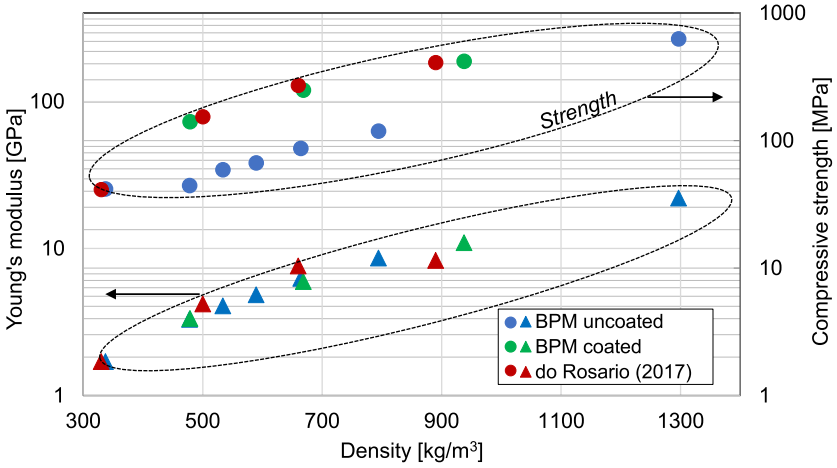

Fig. 15. Young's modulus and compressive strength versus density of pure silica inverse opals and titania coated silica inverse opals. Whereas the Young's modulus of titania coated opals does not improve for the stiffness as a function of density it improves the compressive strength by a factor which varies from 2 to 3.3 depending on coating layer thickness.

the ideal ordering of pores in the FCC packing, which results in a more homogeneous stress distribution.

$$\sigma_{macro} = 576.3 \cdot e^{-3.85 \cdot \epsilon} \tag{26}$$

In Fig. 14.b the dependency of the fractional Young's modulus ($\boldsymbol{E/E_0}$) on porosity is shown and compared to the experimental results of do Rosario et al. [57]. Although the correlation of Wagh et al. [68] was developed for open porosities, it can be effectively applied for regions with low porosities where prevailing closed pores exist. For comparison, Fig. 14 shows the experimental data from Adachi et al. [1] where exponential dependency was observed.

In Fig. 15 the mechanical properties of all investigated structures including samples coated with titania are shown depending on their densities. The densities for experimentally investigated samples were directly measured with four independent measuring techniques [57]. In the case of the BPM simulations, the sample densities were estimated based on the volumetric amount and density of each component. The densities of silica and titania used for the simulations were equal to 1297 kg/m^3 [57] and 3660 kg/m^3 [11] accordingly.

It can be observed, that the coating of samples with an additional titania layer does not allow to significantly improve material stiffness. The coated inverse opals and less porous pure silica samples which have similar densities reveal also similar stiffnesses. For example, the FCC inverse opal coated with 20 nm titania has a density of 668 kg/m^3 and Young's modulus of 5.96 GPa. A pure silica structure with a porosity of 48.8% has a density of 664 kg/m^3 and Young's modulus of 6.26 GPa. However, the additional titania coating has a decisive influence on the compressive strength. It allows to significantly improve material properties. For example, the strength for samples with material density of about 660 kg/m^3 for coated inverse opal is equal to 249 MPa. This value is more than two times larger compared to the strength of pure silica sample, which is equal to 93 MPa.

5. Conclusion

A simulation strategy based on the discrete element method and the bonded-particle model was applied for modeling of inverse opals. Due to the high flexibility of this approach, it was possible to reproduce the internal structure of the simulated material, to consider the effect of an additional coating layer and to analyze the influence of porosity and the pores arrangement. It was shown that BPM-based approach not only allows the macroscopic stress-strain relationships to be extracted from the simulation results, but also can provide a detailed insight into the mechanical response of the structure. Moreover, the explicit solution strategy used in this mesh-free method makes it possible to consider the material fracture on initial stages. However, it should be noted that a simplification has been made in the current study, and solid bonds were modeled by a purely elastic model. This led to discrepancies between experiments and simulations in the region of high strains. For a more accurate reproduction of the material, it is necessary to develop an elastic-plastic model of solid bonds.

The proposed strategy was implemented in the open-source DEM code, and the computations were parallelized for the hybrid CPU-GPU architecture. This allowed to achieve a high-resolution structural model and to effectively perform simulations of scenes consisting of 20-35 million discrete objects.

Analysis of the mechanical behavior of inverse opals under uniaxial loading shows that:

- The material in the struts oriented in the loading direction is compressed, and tensile zones are formed in the interpore openings, as well as at the lower and upper parts of the pores.
- The stresses in the axial direction (perpendicular to the loading direction) are almost four times smaller than in the vertical.
- An additional coating layer of TiO_2 can significantly improve the stiffness and the strength and reduce inhomogeneity of the stress distributions.
- The dependency of the Young's modulus and the strength on porosity can be described using power and exponential functions.

Overall, it can be concluded that the proposed methodology is a very promising approach, which has a very high potential to be applied in similar problems of material science.

Declaration of Competing Interest

The authors declare that they have no known competing financial interests or personal relationships that could have appeared to influence the work reported in this paper.

CRediT authorship contribution statement

Maksym Dosta: Conceptualization, Methodology, Software, Investigation, Writing – original draft, Validation, Visualization, Supervision. **Katrin Bistreck:** Investigation, Validation, Writing – review & editing. **Vasyl Skorych:** Investigation, Software, Writing – review & editing, Validation, Visualization. **Gerold A. Schneider:** Writing – review & editing, Methodology.

Acknowledgements

Funded by the Deutsche Forschungsgemeinschaft (DFG, German Research Foundation) – Projektnummer 192346071 – SFB 986.

References

[1] Adachi T, Sakka S. Dependence of the elastic moduli of porous silica gel prepared by the sol-gel method on heat-treatment. J Mater Sci 1990;25:4732–7. doi:10.1007/BF01129933.
[2] André D, Jebahi M, Iordanoff I, Charles JL, Néauport J. Using the discrete element method to simulate brittle fracture in the indentation of a silica glass with a blunt indenter. Comput Meth Appl Mech Eng 2013;265:136–47. doi:10.1016/j.cma.2013.06.008.
[3] Agwai A, Guven I, Madenci E. Predicting crack propagation with peridynamics: a comparative study. Int J Fract 2011;171:65–78. doi:10.1007/s10704-011-9628-4.
[4] Bargmann S, Klusemann B, Markmann J, Schnabel JE, Schneider K, Soyarslan C, et al. Generation of 3D representative volume elements for heterogeneous materials: a review. Prog Mater Sci 2018;96:322–84. doi:10.1016/j.pmatsci.2018.02.003.
[5] Bauer J, Hengsbach S, Tesari I, Schwaiger R, Kraft O. High-strength cellular ceramic composites with 3D microarchitecture. PNAS 2014;111:2453–8. doi:10.1073/pnas.1315147111.
[6] Bauer J, Schroer A, Schwaiger R, Kraft O. Approaching theoretical strength in glassy carbon nanolattices. Nat Mater 2016;15:438–43. doi:10.1038/nmat4561.
[7] Brown N, Chen J-F, Ooi JY. A bond model for DEM simulation of cementitious materials and deformable structures. Granular Mater 2014;16:299–311. doi:10.1007/s10035-014-0494-4.
[8] Chen X, Wang L, Wen Y, Zhang Y, Wang J, Song Y, et al. Fabrication of closed-cell polyimide inverse opal photonic crystals with excellent mechanical properties and thermal stability. J Mater Chem 2008;18:2262–7. doi:10.1039/b801565a.
[9] Cho H-H, Glazer MPB, Dunand DC. Modeling of stresses and strains during (de)lithiation of Ni3Sn2-coated nickel inverse opal anodes. ACS Appl Mater Interfaces 2017;9:15433–8. doi:10.1021/acsami.7b01640.
[10] Cho Y, Lee SY, Ellerthorpe Feng G, Lin G, Wu G, Yin J, et al. Elastoplastic inverse opals as power-free mechanochromic sensors for force recording. Adv Funct Mater 2015;25:6041–9. doi:10.1002/adfm.201570250.
[11] Colombi P, Bergese P, Bontempi E, Borgese L, Federici S, Keller SS, et al. Sensitive determination of Young's modulus of thin films by polymeric microcantilevers. Meas Sci Tecnol 2013;24. doi:10.1088/0957-0233/24/12/125603.
[12] Cortés C, Osorno M, Uribe D, Steeb H, Ruiz-Salguero O, Barandiarán I, et al. Geometry simplification of open-cell porous materials for elastic deformation FEA. Eng Comput 2019;35:257–76. doi:10.1007/s00366-018-0597-3.
[13] Daxner T. Finite element modeling of cellular materials. Altenbach H., Öchsner A. (eds) Cellular and Porous Materials in Structures and Processes. CISM Int Centre Mech Sci 2010;521. doi:10.1007/978-3-7091-0297-8_2.
[14] Dosta M, Dale S, Antonyuk S, Wassgren C, Heinrich S, Litster JD. Numerical and experimental analysis of influence of granule microstructure on its compression breakage. Powder Technol 2016;299:87–97. doi:10.1016/j.powtec.2016.05.005.
[15] Dosta M, Jarolin K, Gurikov P. Modelling of mechanical behavior of biopolymer alginate aerogels using the bonded-particle model. Molecules 2019;24(14):2543. doi:10.3390/molecules24142543.
[16] Dosta M, Furlan K, Skorych V, Heinrich S, Janssen R. Influence of pores arrangement on stability of photonic structures during sintering. J Eur Cer Soc 2020;40(13):4562–71. doi:10.1016/j.jeurceramsoc.2020.04.019.
[17] Dosta M, Skorych V. MUSEN: an open-source framework for GPU-accelerated DEM simulations. SoftwareX 2020;12. doi:10.1016/j.softx.2020.100618.
[18] Drugan WJ, Willis JR. A micromechanics-based nonlocal constitutive equation and estimates of representative volume element size for elastic composites. J Mech Phys Solids 1996;44:497–524. doi:10.1016/0022-5096(96)00007-5.
[19] Estay D, Chacana F, Ibarra J, Pèrez L, Lascano S. Bond calibration method for Young's modulus determination in the discrete element method framework. Granular Matter 2017;19:60. doi:10.1007/s10035-017-0734-5.
[20] Gao H. Application of fracture mechanics concepts to hierarchical biomechanics of bone and bone-like materials. Int J Fract 2006;138:101–37. doi:10.1007/s10704-006-7156-4.
[21] Giannakeas IN, Papathanasiou TK, Fallah AS, Bahai H. Coupling XFEM and peridynamics for brittle fracture simulation—part I: feasibility and effectiveness. Comput Mech 2020;66:103–22. doi:10.1007/s00466-020-01843-z.
[22] Gibson LJ, Ashby MF. Cellular solids. Cambridge Univ Press; 1997.
[23] Hanley KJ, O'Sullivan C, Oliveira JC, Cronin K, Byrne EP. Application of Taguchi methods to DEM calibration of bonded agglomerates. Powder Techn 2011;210:230–40. doi:10.1016/j.powtec.2011.03.023.
[24] Hatton B, Mischchenko L, Davis S, Sandhage KH, Aizenberg J. Assembly of large-area, highly ordered, crack-free inverse opal films. PNAS 2010;107(23):10354–9. doi:10.1073/pnas.1000954107.
[25] Herakovich CT, Baxter SC. Influence of pore geometry on the effective response of porous media. J Mater Sci 1999;34:1595–609. doi:10.1023/A:1004528600213.
[26] Heydari A, Vahidifar A, Esmizadeh E, Rodrigue D. Experimental and finite element simulation of natural rubber foams using real 3D structures. Polymer 2020;107. doi:10.1016/j.polymer.2020.122505.
[27] Hill BR. Elastic properties of reinforce solids: Some theoretical principles. J. Mech Phys Solids 1963;11:357–72. doi:10.1016/0022-5096(63)90036-X.
[28] Hu Y, Fang Q-Z, Qian J. Effect of cell structure on the uniaxial compression properties of closed-cell foam materials. Mater Today Commun 2021;26. doi:10.1016/j.mtcomm.2021.102104.
[29] Iwai T, Hong C-W, Greil P. Fast particle pair detection algorithms for particle simulations. Int J Mod Phys C 1999;10:823–37. doi:10.1142/S0129183199000644.
[30] Jang D, Meza LR, Greer F, Greer JR. Fabrication and deformation of three-dimensional hollow ceramic nanostructures. Nat Mater 2013;12:893–8. doi:10.1038/nmat3738.
[31] Jarolin K, Dosta M. Linearization-based methods for the calibration of bonded-particle model. Comput Part Mech 2020. doi:10.1007/s40571-020-00348-z.
[32] Jauffrés D, Martin CL, Lichtner A, Bordia RK. Simulation of the elastic properties of porous ceramics with realistic microstructure. Model Simul Mater Sci Eng 2012;20 045009. doi:10.1088/0965-0393/20/4/045009.
[33] Jauffrés D, Martin CL, Bordia RK. Design of strain tolerant porous microstructures – a case of controlled imperfection. Acta Materialia 2018;148:193–201. doi:10.1016/j.actamat.2017.12.039.
[34] Jeon I, Asahina T, Kang K-J, Im S, Lu TJ. Finite element simulation of the plastic collapse of closed-cell aluminum foams with X-ray computed tomography. Mech Mater 2010;42:227–36. doi:10.1016/j.mechmat.2010.01.003.
[35] Jiang S, Ye Y, Li X, Liu S, Liu J, Yang D, et al. DEM modeling of crack coalescence between two parallel flaws in SiC ceramics. Ceram Int 2019;45(12):14997–5014. doi:10.1016/j.ceramint.2019.04.237.
[36] Joannopolous JD, Villeneuve PR, Fan S. Photonic crystals: putting a new twist on light. Nature 1997;386:143–9. doi:10.1038/386143a0.
[37] Kirca M, Gül A, Ekinci E, Yardim F, Mugan A. Computational modeling of micr-cellular carbon foams. Finite Elem. Anal Des 2007;44:45–52. doi:10.1016/j.finel.2007.08.008.
[38] Konstantinidis IC, Papadopoulos DP, Lefakis H, Tsipas DN. Model for determining mechanical properties of aluminum closed-cell foams. Theor Appl Fract Mech 2005;43:157–67. doi:10.1016/j.tafmec.2005.01.001.
[39] Kozhar S, Dosta M, Antonyuk S, Heinrich S, Bröckel U. DEM simulations of amorphous irregular shaped micrometer-sized titania agglomerates at compression. Adv Powd Techn 2015;26(3):767–77. doi:10.1016/j.apt.2015.05.005.
[40] Kubair DV, Ghosh S. Exterior statistics based boundary conditions for establishing statistically equivalent representative volume elements of statistically non-homogeneous elastic microstructures. Int J Solids Struct 2017;112(1):106–21. doi:10.1016/j.ijsolstr.2017.02.015.
[41] Lázaro J, Solórzano E, Rodríguez-Pérez MA, Kennedy AR. Effect of solidification rate on pore connectivity of aluminium foams and its consequences on mechanical properties. Mater Sci Eng A 2016;672:236–46. doi:10.1016/j.msea.2016.07.015.

[42] Luxner MH, Stampfl J, Pettermann HE. Numerical simulations of 3D open cell structures – influence of structural irregularities on elasto-plasticity and deformation localization. Int J Solids Struct 2007;44:2990–3003. doi:10.1016/j.ijsolstr.2006.08.039.
[43] Meza LR, Zelhofer AJ, Clarke N, Mateos AJ, Kochmann DM, Greer JR. Resilient 3D hierarchical architected metamaterials. PNAS 2015;112:11502–7. doi:10.1073/pnas.1509120112.
[44] Mindlin RD, Deresiewicz H. Elastic spheres in contact under varying oblique forces. ASME J Appl Mech 1953;20:327–40.
[45] Nitka M, Tejchman J. Modeling of concrete behavior in uniaxial compression and tension with DEM. Granular Matter 2015;17(1):145–64. doi:10.1007/s10035-015-0546-4.
[46] Orowan E. Fracture and strength of solids. Rep Prog Phys 1949;12. doi:10.1088/0034-4885/12/1/309.
[47] Pèrez L, Lascano S, Aguilar C, Estay D, Messner U, Figueroa IA, et al. DEM-FEA estimation of pores arrangement effect on the compressive Young's modulus for Mg foams. Comput Mater Sci 2015;110:281–6. doi:10.1016/j.commatsci.2015.08.042.
[48] Pikul JP, Özerinc S, Liu B, Zhang R, Braun PV, Deshpande King WP. High strength metallic wood from nanostructured nickel inverse opal materials. Sci Rep 2019;9:719. doi:10.1038/s41598-018-36901-3.
[49] Polanyi M. Über die Natur des Zerreißvorganges. Z. Physik 1921;7:323–7. doi:10.1007/BF01332803.
[50] Potyondy DO, Cundall PA. A bonded-particle model for rock. Int J Rock Mech Min Sci 2004;41(8):1329–64. doi:10.1016/j.ijrmms.2004.09.011.
[51] Potyondy DO. The bonded-particle model as a tool for rock mechanics research and application: current trends and future directions. Geosyst Eng 2015;18(1):1–28. doi:10.1080/12269328.2014.998346.
[52] Quentrec B, Brot C. New method for searching for neighbors in molecular dynamics computations. J Comput Phys 1973;13(3):430–2. doi:10.1016/0021-9991(73)90046-6.
[53] Rice RW. Microstructure dependence of mechanical behavior of ceramics. Treatise Mater Sci Technol 1977;11:199–381. doi:10.1016/B978-0-12-341811-1.50010-8.
[54] Roa JJ, Coll A, Bermejo S, Jimenez-Pique E, Alcubilla R, Castañer L, et al. Mechanical properties of Al_2O_3 inverse opals by means of nanoindentation. J Phys D 2016;49:455303. doi:10.1088/0022-3727/49/45/455303.
[55] Rybczyński S, Dosta M, Schaan G, Ritter M, Schmidt-Döhl F. Numerical study on the mechanical behavior of ultrahigh performance concrete using a three-phase discrete element model. Struct Concrete 2020. doi:10.1002/suco.202000435.
[56] do Rosário JJ, Lilleodden ET, Waleczek M, Kubrin R, Petrov AY, Dyachenko PN, et al. Self-assembled ultra high strength, ultra stiff mechanical metamaterials based on inverse opals. Adv Eng Mat 2015;17:1420–4 https://doi.org/10.1002/adem.201500118.
[57] do Rosário JJ, Berger JB, Lilleodden ET, McMeeking RM, Schneider GA. The stiffness and strength of metamaterials based on the inverse opal architectures. Extreme Mech Lett 2017;12:86–96. doi:10.1016/j.eml.2016.07.006.
[58] do Rosário JJ, Häntsch J, Schneider GA, Lilleodden ET. A combined compression and indentation study of mechanicalmetamaterials based on inverse opal coatings. Acta Materialia 2020;195:98–108. doi:10.1016/j.actamat.2020.04.025.
[59] Schröder J. A numerical two-scale homogenization scheme: FE2-method. Plasticity and beyound. Schröder J, Hackl K, editors. Springer Vienna; 2014. doi:10.1007/978-3-7091-1625-8_1.
[60] Shan J, Du Y, Fan D, Guo L. Determination of parameters of the discrete element bond model for asphalt mixture based on splitting test. Adv Civil Eng 2019;1:1–12. doi:10.1155/2019/5047214.
[61] Shklover V, Braginsky L, Witz G, Mishrikey M, Hafner C. High-temperature photonic structures. Thermal barrier coatings, infrared sources and other applications. J Comput Theor Nanosci 2008;5:862–93. doi:10.1166/jctn.2008.2532.
[62] Spriggs RM, Brissette LA. Expressions for shear modulus and poisson's ratio of porous refractory oxides. J. Am Cer Soc 1962;45:198–9. doi:10.1111/j.1151-2916.1962.tb11121.x.
[63] Stein A, Wiloson BE, Rudisill SG. Design and functionality of colloidal-crystal-templated materials – chemical applications of inverse opals. Chem Soc Rev 2013;42:2763. doi:10.1039/C2CS35317B.
[64] O'Sullivan C, Bray JD. Selecting a suitable time step for discrete element simulations that use the central difference integration scheme. Eng Comput 2003;21:278–303. doi:10.1108/02644400410519794.
[65] Tsoungui O, Vallet D, Charmet J-C. Numerical model of crushing of grains inside two-dimensional granular materials. Powder Techn 1999;199:190–8. doi:10.1016/S0032-5910(99)00137-0.
[66] Tsuji J, Tanaka T, Ishida T. Lagrangian numerical simulation of plug flow of cohesionless particles in a horizontal pipe. Powder Techn 1992;71:239–50. doi:10.1016/0032-5910(92)88030-L.
[67] Verlet L. Computer experiments on classical fluids. I thermodynamical properties of Lennard-Jones molecules. Phys Rev 1967;159:98–103. doi:10.1103/PhysRev.159.98.
[68] Wagh AS, Poeppel RB, Singh JP. Open pore description of mechanical properties of ceramics. J Mater Sci 1991;26:3862–8. doi:10.1007/BF01184983.
[69] Xia Y, Lai Z, Westover T, Klinger J, Huang H, Chen Q. Discrete element modeling of deformable pinewood chips in cyclic loading test. Powder Techn 2019;345:1–14. doi:10.1016/j.powtec.2018.12.072.
[70] Xie D, Waas AM. Discrete cohesive zone model for mixed-mode fracture using finite element analysis. Eng Fract Mech 2006;73:1783–96.
[71] Youssef S, Maire E, Gaertner R. Finite element modelling of the actual structure of cellular materials determined by X-ray tomography. Acta Materialia 2005;53:719–30. doi:10.1016/j.actamat.2004.10.024.
[72] Yoon J. Application of experimental design and optimization to PFC model calibration in uniaxial compression simulation. Int J Rock Mech Min Sci 2007;44:871–89. doi:10.1016/j.ijrmms.2007.01.004.